



Role of interlayer coupling in second harmonic generation in bilayer transition metal dichalcogenides

Xiao Jiang ¹, Lei Kang,² and Bing Huang ^{1,3,*}

¹Beijing Computational Science Research Center, Beijing 100193, China

²Technical Institute of Physics and Chemistry, Chinese Academy of Sciences, Beijing 100190, China

³Department of Physics, Beijing Normal University, Beijing 100875, China



(Received 18 September 2021; revised 5 January 2022; accepted 7 January 2022; published 18 January 2022)

Little is known about the role of weak interlayer coupling in the second harmonic generation (SHG) effects of two-dimensional van der Waals (vdW) systems. In this paper, taking homobilayer MoS₂/MoS₂ and heterobilayer MoS₂/MoSe₂ as typical examples, we have systemically investigated their SHG susceptibilities $\chi^{(2)}$ as a function of interlayer hopping strength (t_{int}) using first-principles calculations. For the $\chi_{\text{yyy}}^{(2)}(0; 0, 0)$ of both MoS₂/MoS₂ and MoS₂/MoSe₂, although the increase of t_{int} can increase the intensities of interlayer optical transitions (IOT), the increased band repulsion around the Γ point can eventually decrease their $\chi_{\text{yyy}}^{(2)}(0; 0, 0)$ values; the larger the t_{int} , the smaller the $\chi_{\text{yyy}}^{(2)}(0; 0, 0)$. For the $|\chi_{\text{yyy}}^{(2)}(-2\omega; \omega, \omega)|$ spectra of MoS₂/MoSe₂ in the low photon-energy region, opposite to the MoS₂/MoS₂, their peak values are very sensitive to the variable t_{int} , due to the strong t_{int} -dependent IOT dominating in the band edge; the larger the t_{int} , the larger the $|\chi_{\text{yyy}}^{(2)}(-2\omega; \omega, \omega)|$. For the $|\chi_{\text{yyy}}^{(2)}(-2\omega; \omega, \omega)|$ of MoS₂/MoS₂ in the high photon-energy region, comparing to the MoS₂/MoSe₂, their peak values will decrease in a much more noticeable way as the t_{int} increases, due to the larger reduction of band-nesting effect. Our study not only can successfully explain the puzzling experimental observations for the different SHG responses in different bilayer transition metal dichalcogenides under variable t_{int} , but also may provide a general understanding for designing controllable the SHG effects in the vdW systems.

DOI: [10.1103/PhysRevB.105.045415](https://doi.org/10.1103/PhysRevB.105.045415)

I. INTRODUCTION

Two-dimensional (2D) layered materials are promising to extend the functionalities from bulk to nanoscale thickness [1–3]. Among them, the noncentrosymmetric materials with large second-order optical susceptibilities, e.g., optical second harmonic generation (SHG) [4–6], linear electro-optic or Pockels effects, sum frequency generation, and optical rectification [7], are highly valuable for various practical applications, e.g., electro-optic modulators, frequency conversion, structure and magnetic orders probing [8–10]. Recently, many monolayer 2D materials have been discovered to exhibit large second or third harmonic generations, including several transition metal dichalcogenides (TMDs) (e.g., MoS₂ [11–15], MoSe₂ [16–18], WS₂ [19,20], and WSe₂ [21]), hexagonal BN [22], InSe [23], and GaSe [24]. Interestingly, despite their monolayer thickness, their effective SHG responses are comparable to many widely used bulk nonlinear optical (NLO) materials [13]. Benefiting from their nanoscale thickness, these 2D systems are promising for on-chip applications without the requirement of phase-matching conditions [8,25].

van der Waals (vdW) engineering has been widely applied to manipulate the electronic and optoelectronic properties of 2D materials. For example, the vdW homobilayer (e.g., MoS₂/MoS₂ [26,27] and bilayer graphene [28–30]) and heterobilayer (e.g., MoS₂/MoSe₂ [26,31–33] and graphene/h-BN

[34]) structures can exhibit fundamentally different electronic and optical properties compared to their individual components [27], due to the existence of weak interlayer coupling effects. In practice, the interlayer coupling strength of these vdW bilayers can be either enhanced by the external pressure/postannealing [26,35–37] or decreased by the wide band-gap thin films inserted/dry transferred [26]. Surprisingly, it is found that depending on the different types of TMDs, the SHG responses in these systems can be either sensitive (e.g., in heterobilayers) or insensitive (e.g., in homobilayers) to the variable interlayer coupling strengths [26]. However, until now, it is still unclear about the physical origin behind these puzzling experimental observations, preventing the design of controllable SHG effects in the 2D systems.

In this paper, taking homobilayer MoS₂/MoS₂ and heterobilayer MoS₂/MoSe₂ as the typical examples, we have systemically investigated the SHG susceptibilities $\chi^{(2)}$ of these bilayer TMDs as a function of interlayer hopping strength (t_{int}) using first-principles Wannier function calculations. Interestingly, for the $\chi_{\text{yyy}}^{(2)}(0; 0, 0)$, it is found that although the increase of t_{int} can increase the interlayer optical transitions, the increased band repulsion around the Γ point in the band structures of both MoS₂/MoS₂ and MoS₂/MoSe₂ can largely decrease their $\chi_{\text{yyy}}^{(2)}(0; 0, 0)$ values. The larger the t_{int} , the smaller the $\chi_{\text{yyy}}^{(2)}(0; 0, 0)$. For the $|\chi_{\text{yyy}}^{(2)}(-2\omega; \omega, \omega)|$ spectra of bilayer MoS₂/MoSe₂, it is found that the intensities of low photon-energy peaks are insensitive to the variable t_{int} , but the intensities of high photon-energy peaks will gradually decrease as the t_{int} increases, due to the reduced band-nesting effect. Differing from the bilayer MoS₂/MoS₂,

*Bing.Huang@csrsc.ac.cn

it is found that the intensities of low photon-energy peaks in the $|\chi_{yyy}^{(2)}(-2\omega; \omega, \omega)|$ spectra of MoS₂/MoSe₂ can significantly increase as the t_{int} increases, due to the strongly enhanced band-edge optical transitions, but the intensities of high photon-energy peaks will decrease as the t_{int} increases, which is less noticeable than that in the MoS₂/MoS₂. Our findings not only can well explain the puzzling experimental observations for the different SHG responses in the homo- and heterobilayer TMDs under variable interlayer coupling strengths, but also could be important for designing tunable SHG effects in other 2D vdW systems.

II. METHODS

A. SHG calculations

The SHG susceptibility tensor $\chi_{\text{total}}^{abc}(-2\omega; \omega, \omega)$ can be calculated as [38,39]

$$\chi_{\text{total}}^{abc}(-2\omega; \omega, \omega) = \chi_e^{abc} + \chi_i^{abc}. \quad (1)$$

In Eq. (1), the χ_e^{abc} and χ_i^{abc} terms originate from the interband contribution and the mixed interband and intraband contributions, respectively, which can be written as

$$\chi_e^{abc}(-2\omega; \omega, \omega) = \frac{e^3}{\hbar^2 \Omega} \sum_{nml,k} \frac{r_{nm}^a \{r_{ml}^b r_{ln}^c\}}{(\omega_{ln} - \omega_{ml})} \left[\frac{2f_{nm}}{\omega_{mn} - 2\omega} + \frac{f_{ln}}{\omega_{ln} - \omega} + \frac{f_{ml}}{\omega_{ml} - \omega} \right] \quad (2)$$

and

$$\begin{aligned} \chi_i^{abc}(-2\omega; \omega, \omega) = & \frac{i}{2} \frac{e^3}{\hbar^2 \Omega} \sum_{nml,k} \frac{2}{\omega_{mn}(\omega_{mn} - 2\omega)} r_{nm}^a (r_{nm;c}^b + r_{mn;b}^c) + \frac{1}{\omega_{mn}(\omega_{mn} - \omega)} (r_{nm;c}^a r_{mn}^b + r_{nm;b}^a r_{mn}^c) \\ & + \frac{1}{\omega_{mn}^2} \left(\frac{1}{\omega_{mn} - \omega} - \frac{4}{\omega_{mn} - 2\omega} \right) r_{nm}^a (r_{nm}^b \Delta_{mn}^c + r_{mn}^c \Delta_{mn}^b) - \frac{1}{2\omega_{mn}(\omega_{mn} - \omega)} (r_{nm;a}^b r_{mn}^c + r_{nm;a}^c r_{mn}^b). \end{aligned} \quad (3)$$

In Eqs. (2) and (3), the $f_{nm} = f_n - f_m$, $\omega_{nm} = \omega_n - \omega_m$, and $\Delta_{nm} = v_{nm} - v_{mn}$ are the Fermi distribution function difference, energy difference, and electron group velocity difference between the n th and m th bands, respectively. The r_{nm} is the position operator $r_{nm} = \frac{v_{nm}}{i\omega_{nm}}$, representing the optical transition dipole moments (TDMs) between n th and m th bands. The Ω is the volume of unit cell, and $\{r_{ml}^b r_{ln}^c\}$ is defined as $1/2(r_{nl}^b r_{lm}^a + r_{nl}^a r_{lm}^b)$. The $r_{nm;a}^b$ is the generalized derivative of the coordinate operator in momentum space with the form of

$$r_{nm;b}^a = \frac{i}{\omega_{nm}} \left[\frac{v_{nm}^a \Delta_{nm}^b + v_{nm}^b \Delta_{nm}^a}{\omega_{nm}} - W_{nm}^{ab} + \sum_{p \neq n,m} \left(\frac{v_{np}^a v_{pm}^b}{\omega_{pm}} - \frac{v_{np}^b v_{pm}^a}{\omega_{np}} \right) \right], \quad (4)$$

where $W_{nm}^{ab} = \langle n | \partial_{k_a} \partial_{k_b} H | m \rangle$ [40,41]. In practical calculations, the frequency ω in the denominator of SHG susceptibility tensor has a small imaginary smearing factor δ ($\omega \rightarrow \omega + i\delta$), and $\delta = 0.05$ eV is used in this study (see Fig. S1(a) [42] for the test about δ).

At zero-frequency limit ($\omega = 0$), the value of $\chi_{\text{total}}^{abc}(-2\omega; \omega, \omega)$, i.e., $\chi_{\text{total}}^{abc}(0; 0, 0)$, can be reduced to

$$\chi_e^{abc} = \frac{e^3}{\hbar^2 \Omega} \sum_{nml,k} \frac{r_{nm}^a \{r_{ml}^b r_{ln}^c\}}{\omega_{nm} \omega_{ml} \omega_{ln}} [\omega_n f_{ml} + \omega_m f_{ln} + \omega_l f_{nm}] \quad (5)$$

and

$$\chi_i^{abc} = \frac{i}{4} \frac{e^3}{\hbar^2 \Omega} \sum_{nml,k} \frac{f_{nm}}{\omega_{mn}^2} [r_{nm}^a (r_{nm;c}^b + r_{mn;b}^c) + r_{nm}^b (r_{mn;c}^a + r_{mn;a}^c) + r_{nm}^c (r_{mn;b}^a + r_{mn;a}^b)]. \quad (6)$$

The $\chi_{\text{total}}^{abc}(0; 0, 0)$ is an important physical quantity for evaluating the intrinsic SHG properties of a system.

The general expression of SHG susceptibility $\chi_{abc}^{(2)}(-2\omega; \omega, \omega)$ can be simplified as

$$\chi_{abc}^{(2)}(-2\omega; \omega, \omega) = \sum_{nml,k} A_{nml}(\mathbf{k}, \omega). \quad (7)$$

To obtain the band-resolved SHG susceptibility tensor, it can be decomposed into the individual bands by partially summing only two out of all the three bands indices [43]. For example, the resolved SHG susceptibility for the n th band can be written as

$$\chi_{abc,nk}^{(2)}(-2\omega; \omega, \omega) = \sum_{ml} A_{nml}(\mathbf{k}, \omega). \quad (8)$$

Moreover, the SHG susceptibility tensor can be projected to the full Brillouin zone by summing over all the three bands indices [44]:

$$\chi_{abc,k}^{(2)}(-2\omega; \omega, \omega) = \sum_{nml} A_{nml}(\mathbf{k}, \omega). \quad (9)$$

Here, the definition of $A_{nmi}(\mathbf{k}, \omega)$ with the form of

$$\begin{aligned}
 A_{nmi}^{abc}(\mathbf{k}, \omega) = & \frac{e^3}{\hbar^2 \Omega} \frac{r_{nm,k}^a \{r_{ml,k}^b r_{ln,k}^c\}}{(\omega_{ln,k} - \omega_{ml,k})} \left[\frac{2f_{nm,k}}{\omega_{mn,k} - 2\omega} + \frac{f_{ln,k}}{\omega_{ln,k} - \omega} + \frac{f_{ml,k}}{\omega_{ml,k} - \omega} \right] + \frac{i}{2} \frac{e^3}{\hbar^2 \Omega} \left[\frac{2}{\omega_{mn,k}(\omega_{mn,k} - 2\omega)} r_{nm,k}^a (r_{nm;c,k}^b + r_{mn;b,k}^c) \right. \\
 & + \frac{1}{\omega_{mn,k}(\omega_{mn,k} - \omega)} (r_{nm;c,k}^a r_{mn,k}^b + r_{nm;b,k}^a r_{mn,k}^c) + \frac{1}{\omega_{mn,k}^2} \left(\frac{1}{\omega_{mn,k} - \omega} - \frac{4}{\omega_{mn,k} - 2\omega} \right) r_{nm,k}^a (r_{nm,k}^b \Delta_{mn,k}^c + r_{mn,k}^c \Delta_{mn,k}^b) \\
 & \left. - \frac{1}{2\omega_{mn,k}(\omega_{mn,k} - \omega)} (r_{nm;a,k}^b r_{mn,k}^c + r_{nm;a,k}^c r_{mn,k}^b) \right]. \quad (10)
 \end{aligned}$$

All the above SHG-related calculations are performed in our homemade NOPSS package, which can be used to calculate the SHG susceptibility, shift/injection current, and plasmonic excitation [45,46]. The parameters used in our NOPSS package can be accepted from either the first-principles calculations or tight-binding calculations.

B. First-principles calculations

The first-principles based density-functional theory (DFT) calculations are performed using the Vienna *Ab initio* Simulation Package (VASP) [47]. The pseudopotentials of the projector augmented-wave type are adopted to describe the interaction between valence electrons and ionic cores [48]. The exchange-correlation energy is treated within the generalized gradient approximation as parametrized by Perdew, Burke, and Ernzerhof (PBE) [49]. The energy cutoff of 500 eV and Monkhorst-Pack k -point meshes of $15 \times 15 \times 1$ in the 2D Brillouin zone are adopted in our study, which can be used to obtain the converged results. The convergence criteria for force and energy are set to be 1×10^{-3} eV and 1×10^{-5} eV/Å, respectively. The vacuum layer is set to 30 Å, which is sufficiently large to avoid the artificial interlayer coupling between the neighboring supercells. The vdW interactions of the 2D systems are treated by the DFT-D3 method [50].

Because of the ill-defined thickness of 2D systems, the calculated SHG susceptibility should be renormalized [51,52]. Similar to the sheet conductance of 2D materials, we define the 2D SHG susceptibility as $\chi_{\text{sheet}}^{\text{SHG}}(-2\omega; \omega, \omega) = \chi_{\text{bulk}}^{\text{SHG}}(-2\omega; \omega, \omega) \times L_z$ [48]. Here, L_z is the length of the entire unit cell along the vacuum direction [5]. Therefore, based on this definition, the unit of sheet SHG susceptibility is pm^2/V .

The Wannier fitting of DFT band structure is implemented within the WANNIER90 code [53], in which the Hamiltonian in Wannier basis can be constructed to obtain the r_{nm} for the SHG calculations. The Hamiltonian for bilayer TMDs can be written as

$$\begin{aligned}
 \hat{H}^{(2L)} = & \sum_k [\hat{\phi}_1^\dagger(k) H_1^{(1L)} \hat{\phi}_1(k) + \hat{\phi}_2^\dagger(k) H_2^{(1L)} \hat{\phi}_2(k) \\
 & + \hat{\phi}_2^\dagger(k) V_{\text{int}}^{(LL)} \hat{\phi}_1(k) + \text{H.c.}], \quad (11)
 \end{aligned}$$

where $H_1^{(1L)}$ and $H_2^{(1L)}$ are the Hamiltonian of the individual monolayer TMDs, and $\hat{\phi}_1(k)$ and $\hat{\phi}_2(k)$ are their corresponding wave functions. As shown in Eq. (11), the interlayer interactions in bilayer TMDs can be introduced by $V_{\text{int}}^{(LL)}$. In our study, the interlayer hopping strengths t_{int} in $V_{\text{int}}^{(LL)}$ can be artificially tuned to different values to simulate the different

interlayer coupling strengths. Meanwhile, the different interlayer distances (d_{int}) corresponding to the different t_{int} can be calculated via comparing their band structures. In particular, $t_{\text{int}} = t_0$ is defined as the interlayer coupling strength of bilayer TMDs at the equilibrium interlayer distance.

III. RESULT AND DISCUSSION

In Secs. III A and III B, we will discuss the role of t_{int} in the SHG responses in the homobilayer MoS₂/MoS₂ systems, respectively. In Secs. III C and III D, we will discuss the role of t_{int} in the SHG responses in the heterobilayer MoS₂/MoS₂ systems, respectively. Since the SHG effects can only exist in the systems without inversion symmetry, the bilayer TMD systems with 3R type are considered, which have been synthesized in the prior experiments [12,26].

A. $\chi_{yyy}^{(2)}(\mathbf{0}; \mathbf{0}, \mathbf{0})$ of the homobilayer MoS₂/MoS₂ as a function of t_{int}

The structure of bilayer MoS₂/MoS₂ in 3R phase ($R3m$) is shown as the inset of Fig. 1(b). For the bilayer MoS₂/MoS₂ with decoupled interlayer coupling effect, i.e., $t_{\text{int}} = 0$, it is a direct band-gap (E_g) semiconductor (DFT-calculated $E_g = 1.7$ eV) with both conduction-band minimum (CBM) and valence-band maximum (VBM) locating at the K point, same as the monolayer MoS₂ [15]. Due to the strong spin-orbital coupling (SOC) effect, the double-degenerated CBM or VBM in each MoS₂ layer will split into two single ones with opposite spin directions at the K point [15]. As shown in Fig. 1(a), the orbital-resolved band structure shows that the CBM and VBM are mostly contributed by the Mo d_{z^2} and Mo $d_{x^2-y^2} + d_{xy}$ orbitals, respectively.

As shown in Fig. 1(c), when t_{int} increases from 0 to t_0 (the hopping strength at the equilibrium interlayer distance $d_{\text{int}} = 3.0$ Å), the interlayer coupling effect can significantly modulate the band structure of MoS₂/MoS₂, especially around the highest-symmetry Γ point, inducing a direct-to-indirect band-gap transition (DFT-calculated $E_g = 1.3$ eV) [27]. Comparing the cases between $t_{\text{int}} = 0$ [Fig. 1(a)] and $t_{\text{int}} = t_0$ [Fig. 1(c)], it is observed that there is a large band repulsion around the Γ point at the top of the valence band, shifting the VBM to the Γ point. Now, the VBM state is contributed by the Mo- d_{z^2} and $S - p_z$ orbitals among the two different layers. Therefore, differing from the simple three-orbital ($d_{z^2}, d_{xy}, d_{x^2-y^2}$) tight-binding model for monolayer MoS₂ [54], the $S p$ orbitals must be included to capture the low-energy band structure of bilayer MoS₂/MoS₂ [55]. Accordingly, to accurately describe the interlayer coupling effect and its role in the SHG

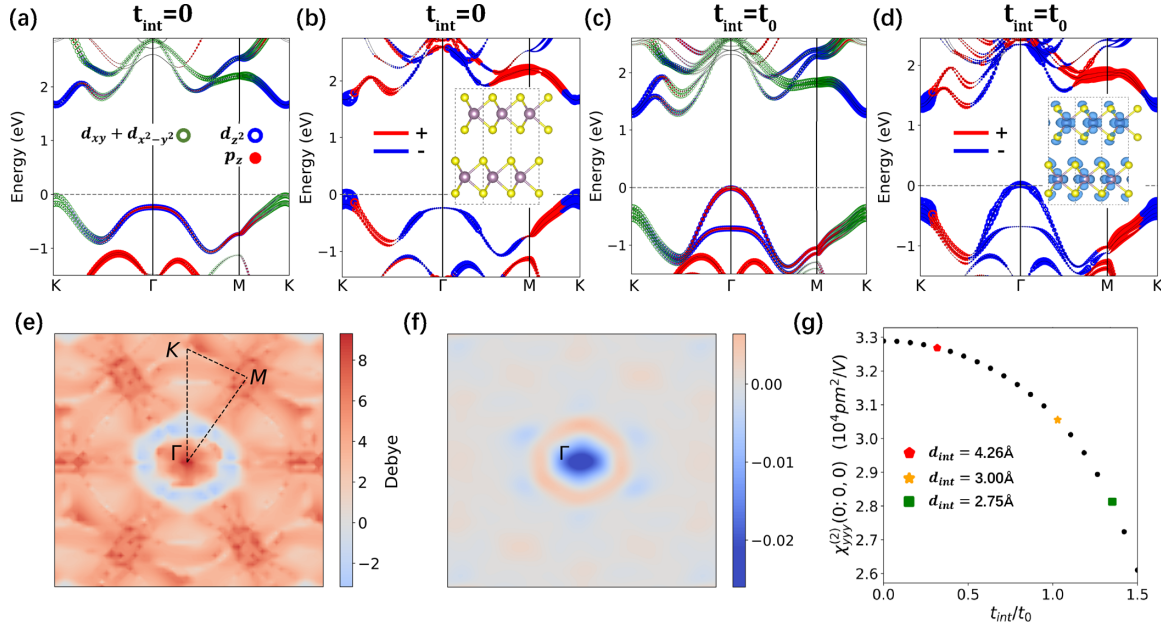


FIG. 1. (a), (b) Orbital-resolved and SHG-weighted band structures of the homobilayer MoS₂/MoS₂ ($t_{\text{int}} = 0$), respectively. SOC effects are considered in the band-structure calculations. Fermi level is set to zero. (b), inset: Side view of the MoS₂/MoS₂ in 3R phase. (c), (d) Same as (a), (b) but for the case of MoS₂/MoS₂ ($t_{\text{int}} = t_0$). (d), inset: SHG-weighted charge density of MoS₂/MoS₂ in the real space. See the enlarged versions of the insets in (b) and (d) in Fig. S2 [42]. (e) Difference of TDMs between the cases of $t_{\text{int}} = 0$ and $t_{\text{int}} = t_0$ in the full BZ for the MoS₂/MoS₂. Here, the plotted TDMs are the sum of all the four optical transition processes between the top two valence bands and the bottom two conduction bands. (f) Difference of SHG projection between the cases of $t_{\text{int}} = 0$ and $t_{\text{int}} = t_0$ for the MoS₂/MoS₂ in the full BZ. (g) Values of SHG susceptibility $\chi_{yyy}^{(2)}(0; 0, 0)$ for the MoS₂/MoS₂ as a function of t_{int} . Three typical d_{int} corresponding to different t_{int} are also shown here.

response, we have constructed the Hamiltonian in Wannier basis using 20 Mo d orbitals and 24 S p orbitals (including the SOC effects) to generate the localized Wannier functions [see Fig. S1(b) [42] for the convergence test of the SHG calculations as a function of energy bands]. Overall, the Wannier fitted band structure agrees well with the DFT one (see Fig. S3 [42]).

When the t_{int} increases, the interlayer wave function overlap can increase, which may give rise to the increased optical transition intensities in the system. By calculating the TDMs between top two valence bands and bottom two conduction bands in the full Brillouin zone (BZ) of MoS₂/MoS₂ under $t_{\text{int}} = 0$ (Fig. S4(a) [42]) and $t_{\text{int}} = t_0$ (Fig. S4(b) [42]), we can obtain the difference between them. As shown in Fig. 1(e), indeed, it is interesting to observe that the optical transition intensities are increasing in the entire BZ except for a small area around the Γ point.

Generally, it is expected that increased TDMs may increase the $\chi^{(2)}$. To test this intuition, we have calculated the $\chi^{(2)}$ of MoS₂/MoS₂. Because of the D_{3h} point-group symmetry, there is only one independent SHG response susceptibility tensor element $\chi_{yyy}^{(2)} = -\chi_{yxx}^{(2)} = -\chi_{xyx}^{(2)} = -\chi_{xyy}^{(2)}$. Surprisingly, it is found that the calculated value of SHG susceptibility $\chi_{yyy}^{(2)}(0; 0, 0)$ decreases (not increases) from 3.3×10^4 to 3.0×10^4 pm²/V when t_{int} increases from 0 to t_0 . The SHG-weighted charge density [inset of Fig. 1(d)] shows that the $\chi_{yyy}^{(2)}(0; 0, 0)$ is mainly contributed by Mo $d_{x^2-y^2} + d_{xy}$, Mo d_{z^2} , and S p_z orbitals, regardless of the specific value of t_{int} .

It is interesting to further understand this unusual mechanism for the reduction of $\chi_{yyy}^{(2)}(0; 0, 0)$ from $t_{\text{int}} = 0$ and $t_{\text{int}} =$

t_0 . Figure 1(b) and Fig. S4(c) [42] show the projections of $\chi_{yyy}^{(2)}(0; 0, 0)$ in the band structure and in the full BZ for the $t_{\text{int}} = 0$ case, respectively. Interestingly, it is shown that the positive (negative) component of $\chi_{yyy}^{(2)}(0; 0, 0)$ is mostly contributed by the energy states around the M (K) point. A similar SHG component distribution is also found in the $t_{\text{int}} = t_0$ case, as shown in Fig. 1(d) and Fig. S4(d) [42]. By calculating the SHG projection in the full BZ of MoS₂/MoS₂ under $t_{\text{int}} = 0$ and $t_{\text{int}} = t_0$, we can obtain the difference between them. As shown in Fig. 1(e), when the t_{int} increases, the negative SHG component mostly increases around the Γ point, consequently decreasing the $\chi_{yyy}^{(2)}(0; 0, 0)$ value. This finding can be further understood by the projection of $\chi_{yyy}^{(2)}(0; 0, 0)$ into each band at each k point in the band structure, as shown in Figs. 1(b) and 1(d). Interestingly, it is observed that this enhanced negative component of $\chi_{yyy}^{(2)}(0; 0, 0)$ from $t_{\text{int}} = 0$ to $t_{\text{int}} = t_0$ is strongly associated with the increased band repulsion around the Γ point around the top valence band, which can effectively reduce the joint density of states (JDOS) at the band edge for optical transitions.

To further understand the role of t_{int} on the $\chi_{yyy}^{(2)}(0; 0, 0)$, we have systematically calculated the $\chi_{yyy}^{(2)}(0; 0, 0)$ as a function of t_{int} from 0 to $1.5t_0$. As shown in Fig. 1(g), it is seen that with the increase of t_{int} , the $\chi_{yyy}^{(2)}(0; 0, 0)$ will gradually decrease from 3.3×10^4 to 2.6×10^4 pm²/V, a large reduction of $\sim 21\%$. The three d_{int} values corresponding to the different t_{int} are also calculated and plotted in Fig. 1(g). With the t_{int} varying from $0.32t_0$ to $1.0t_0$ to $1.34t_0$, the interlayer distance d_{int} decreases from 4.26 to 3.0 to 2.75 Å.

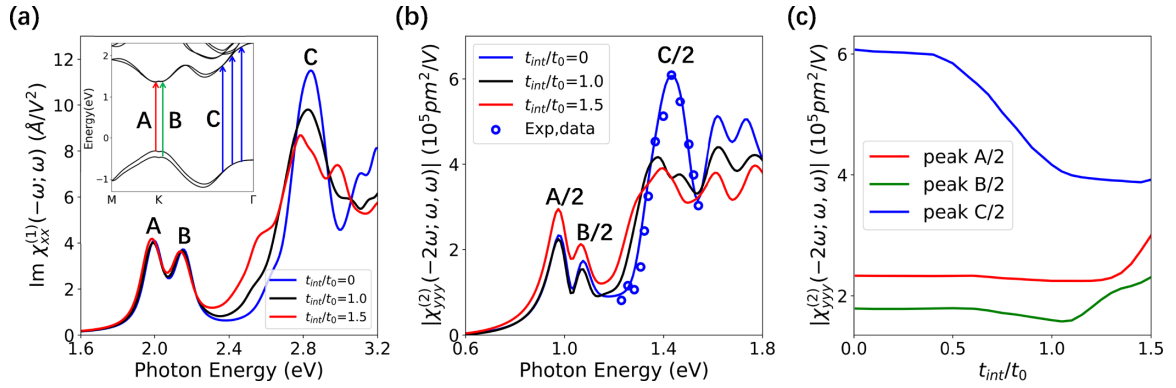


FIG. 2. (a) Linear $\text{Im} \chi^{(1)}(-\omega; \omega)$ (imaginary part of dielectric function) and (b) frequency-dependent SHG susceptibility $|\chi_{yyy}^{(2)}(-2\omega; \omega, \omega)|$ of the homobilayer $\text{MoS}_2/\text{MoS}_2$ under different interlayer hopping strength t_{int} . (a), inset: Arrows indicate the origin of optical transitions in the band structure contributed to A (A/2), B (B/2), and C (C/2) peaks in the $\text{Im} \chi^{(1)}(-\omega, \omega)$ ($|\chi_{yyy}^{(2)}(-2\omega; \omega, \omega)|$) spectra. In (b), blue dots indicate the experimentally measured values (enlarged by $8\times$) for the case of $t_{\text{int}} = 0$, adopted from Ref. [12]. (c) Intensities of A/2, B/2, and C/2 peaks in the $|\chi_{yyy}^{(2)}(-2\omega; \omega, \omega)|$ spectra as a function of t_{int} .

Therefore, we can conclude that although the increase of t_{int} can increase the TDMs, the increased band repulsion around the Γ point in the homobilayer $\text{MoS}_2/\text{MoS}_2$ can eventually decrease $\chi_{yyy}^{(2)}(0; 0, 0)$; the larger the t_{int} , the stronger band repulsion and consequently the smaller the $\chi_{yyy}^{(2)}(0; 0, 0)$ value.

B. $|\chi_{yyy}^{(2)}(-2\omega; \omega, \omega)|$ spectra of the homobilayer $\text{MoS}_2/\text{MoS}_2$ as a function of t_{int}

Besides the value of SHG susceptibility $\chi_{yyy}^{(2)}(0; 0, 0)$, it is interesting to further understand the ω -dependent $\chi_{yyy}^{(2)}(-2\omega; \omega, \omega)$ as a function of t_{int} . Here we focus on the $|\chi_{yyy}^{(2)}(-2\omega; \omega, \omega)|$ spectrum, which is directly associated with the experimentally measured SHG intensities at different ω . Generally, the linear and nonlinear optical spectra are strongly associated. To demonstrate the relationship between $\text{Im} \chi^{(1)}(-\omega; \omega)$ (imaginary part of dielectric function) and $|\chi_{yyy}^{(2)}(-2\omega; \omega, \omega)|$ under different t_{int} , both are calculated. Figure 2(a) shows the calculated $\text{Im} \chi^{(1)}(-\omega; \omega)$ spectra for the $\text{MoS}_2/\text{MoS}_2$. There are three main peaks between 1.8 and 3.0 eV, which are marked as A, B, and C, respectively. As shown in the inset of Fig. 2(a), the A and B peaks are induced by the optical transitions around the band edge at the K point, while the C peak originates from the strong band-nesting effect along part of the K - Γ line [56]. Interestingly, when the t_{int} increases, the intensities of A and B peaks in $\text{Im} \chi^{(1)}(-\omega; \omega)$ are almost unchanged but the intensity of the C peak decreases significantly. This is mostly because the change of t_{int} mostly influences the band structures around the Γ point rather than the K point, as shown in Figs. 1(a) and 1(c). The larger the t_{int} , the larger the band dispersion around the Γ point, consequently, the smaller the JDOS contributed to the optical transitions (Fig. S5(a) [42]). Figure 2(b) shows the calculated $|\chi_{yyy}^{(2)}(-2\omega; \omega, \omega)|$ as a function of t_{int} . The $|\chi_{yyy}^{(2)}(-2\omega; \omega, \omega)|$ involves both single-photon (ω) and double-photon (2ω) resonances. Especially, the energy region of $E < 1.8$ eV (below the band gap of $\text{MoS}_2/\text{MoS}_2$) solely belongs to the double-photon resonance while the energy region of $E > 1.8$ eV (not shown here) belongs to the mix of both single-photon and double-photon resonances. Here we focus on the low photon-

energy region of $E < 1.8$ eV. Therefore, the A/2, B/2, and C/2 peaks shown in Fig. 2(b) all belong to the pure 2ω resonance. Since the energy positions of A/2, B/2, and C/2 peaks in the $|\chi_{yyy}^{(2)}(-2\omega; \omega, \omega)|$ spectra are exactly the half values of the corresponding A, B, and C peaks in the $\text{Im} \chi^{(1)}(-\omega; \omega)$ spectra, they should have the similar origin of optical transitions in the band structure [inset of Fig. 2(a)]. As shown in Fig. 2(b), the spectral position and shape of C/2 peak of bilayer $\text{MoS}_2/\text{MoS}_2$ ($t_{\text{int}} = 0$) at ~ 1.45 eV fits well with the experimentally measured monolayer MoS_2 (marked in blue dots) [12]. We notice that our calculated C/2 peak intensity is roughly $3.7\times$ larger than the experimentally measured one. This difference, as also observed in other study [5,57], may be caused by either some uncertainties in the experiments (e.g., the effect of substrate where substrate phonons or strain may be important) or the underestimation of the smearing factor δ in our calculations, which is related to the electronic relaxation time in the real samples. There have been experimentally measured SHG signals of A/2 and B/2 peaks for $\text{MoS}_2/\text{MoS}_2$ bilayer [26]. Although due to different units, a direct comparison between our calculated values and the experimental data is unlikely; the calculated spectral positions and shapes of A/2 and B/2 peaks are similar to the experimentally measured ones for the decoupled bilayer MoS_2 , as shown in Fig. S6 [42]. As shown in Fig. 2(c), the intensities of A/2 and B/2 peaks will only slightly change as a function of t_{int} . For example, the peak value of A/2 will keep almost unchanged in the region of $0 < t_{\text{int}} < 0.6t_0$, and then slightly decreases from 2.3×10^5 to 2.2×10^5 pm^2/V in the region of $0.6t_0 < t_{\text{int}} < 1.2t_0$, and further increases from 2.2×10^5 to 3.0×10^5 pm^2/V in the region of $1.2t_0 < t_{\text{int}} < 1.5t_0$; however, the intensity of C/2 will largely decrease from 6.0×10^5 to 3.9×10^5 pm^2/V as the t_{int} increases from 0 to $1.5t_0$, a strong reduction of $\sim 35\%$. Our study can well explain the experimental observations that the SHG intensities of A/2 and B/2 peaks in the homobilayer $\text{MoS}_2/\text{MoS}_2$ can only slightly reduce from the decoupled case (inserted by SiO_2 thin film, $t_{\text{int}} \sim 0$) to the equilibrium case ($t_{\text{int}} = t_0$) [26]. Generally, the $\chi^{(2)}$ coefficient for a NLO material can be approximately expressed as

$$\chi_{ijk}^{(2)} = \chi_{ii}^{(1)} \chi_{jj}^{(1)} \chi_{kk}^{(1)} \Delta_{ijk}^{(2)}. \quad (12)$$

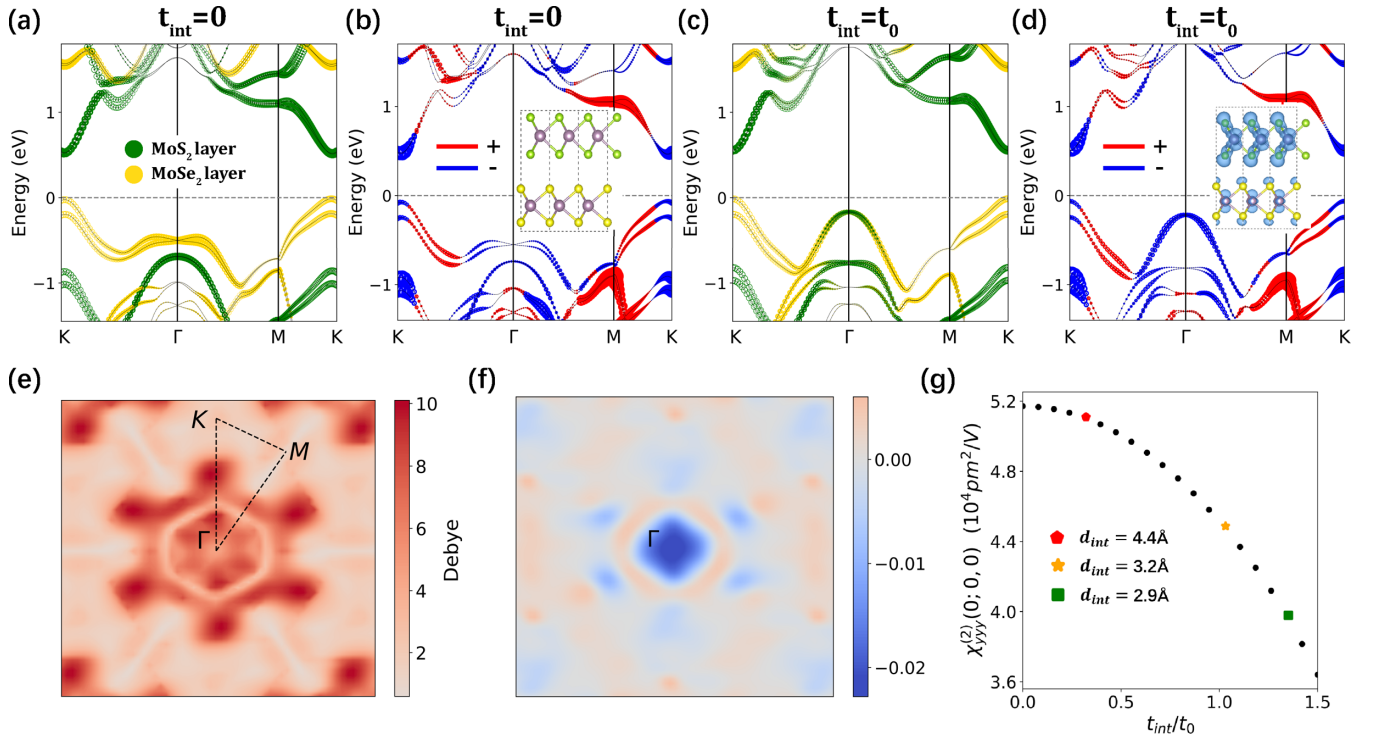


FIG. 3. (a), (b) Orbital-resolved and SHG-weighted band structures of the heterobilayer MoS₂/MoSe₂ ($t_{\text{int}} = 0$), respectively. SOC effects are considered in the band-structure calculations. Fermi level is set to zero. (b), inset: Side view of the atomic structure of MoS₂/MoSe₂. (c), (d) Same as (a), (b) but for the case of MoS₂/MoSe₂ ($t_{\text{int}} = t_0$). (d), inset: SHG-weighted charge density of the MoS₂/MoSe₂ in the real space. See the enlarged versions of the insets in (b) and (d) in Fig. S2 [42]. (e): Difference of TDMs between the cases of $t_{\text{int}} = 0$ and $t_{\text{int}} = t_0$ in the full BZ for the MoS₂/MoSe₂. Here, the plotted TDMs are the sum of all the four optical transition processes between the top two valence bands and the bottom two conduction bands. (f) Difference of SHG projection between the cases of $t_{\text{int}} = 0$ and $t_{\text{int}} = t_0$ for the MoS₂/MoSe₂ in the full BZ. (g) Values of SHG susceptibility $\chi_{\text{yyy}}^{(2)}(0; 0, 0)$ for the MoS₂/MoSe₂ as a function of t_{int} . Three typical d_{int} corresponding to different t_{int} are also shown here.

Here, $\chi^{(1)}$ is the linear susceptibility, and $\Delta_{ijk}^{(2)}$, called the Miller coefficient, is a constant reflecting the intrinsic NLO strength of a system [58]. From the formula above, we can imagine that the SHG intensities could vary more significantly than the linear susceptibility.

We emphasize that, in practice, the exciton effects need to be considered using the accurate *GW* + Bethe-Salpeter equation (BSE) method, in order to capture the realistic optical spectra [15,57]. Fortunately, the underestimation of band gap in the DFT-PBE calculations can accidentally obtain the similar peak positions as the experimental measurements [27]. In fact, there is one pioneering study [57] discussing the influence of exciton effects on SHG response on monolayer MoS₂, using a tight-binding band structure and implementation of excitons in a Bethe-Salpeter framework. According to their findings: (1) the width of A/2 and B/2 peaks [Fig. 2(b)] in the SHG spectrum becomes narrower after the inclusion of exciton effects and the intensity of B/2 peak is slightly enhanced; (2) due to the cancellation of exciton effects and quasiparticle energy shifts, the A/2 and B/2 peak positions are indeed almost unchanged after the inclusion of exciton effects; (3) in the high photon-energy region, e.g., larger than the C/2 peak position, excitonic effects can alter the resonance structure of the SHG spectrum.

C. $\chi_{\text{yyy}}^{(2)}(0; 0, 0)$ of the heterobilayer MoS₂/MoSe₂ as a function of t_{int}

The structure of heterobilayer MoS₂/MoSe₂ in the *3R* phase is shown as inset of Fig 3(b). Due to the lattice mismatch between MoS₂ and MoSe₂, the lattice constant of MoS₂ (MoSe₂) is expanded (compressed) by $\sim 2.8\%$ ($\sim 2.1\%$) to build the small supercell for the convenience of our calculations. For the MoS₂/MoSe₂, due to the different energy levels of anion atomic orbitals, MoS₂ and MoSe₂ can form a type-II band alignment, giving rise to a largely reduced band gap compared to its monolayer components. As shown in Figs. 3(a) and 3(c), the E_g of MoS₂/MoSe₂ are 0.52 and 0.56 eV for the cases of $t_{\text{int}} = 0$ and $t_{\text{int}} = t_0$, respectively. This indicates that the interlayer coupling has little effect on the band-gap values of MoS₂/MoSe₂, differing from the case of MoS₂/MoS₂ where a direct-to-indirect band-gap transition occurs. The band-edge states of MoS₂/MoSe₂ are mainly contributed by the Mo *d* orbitals and Se *p* orbitals. Similar to the case of bilayer MoS₂/MoS₂, we can see that the effect of t_{int} on the band structure mainly reflects in the top valence band around the Γ point, originated from the coupling between Mo *d*_{z² and Se/S *p*_z orbitals between the two neighboring layers. When the t_{int} increases, as a type-II semiconductor, it is expected that the interlayer optical transitions in the MoS₂/MoSe₂ can be significantly increased, which is well confirmed by the calculated TDMs between the top two}

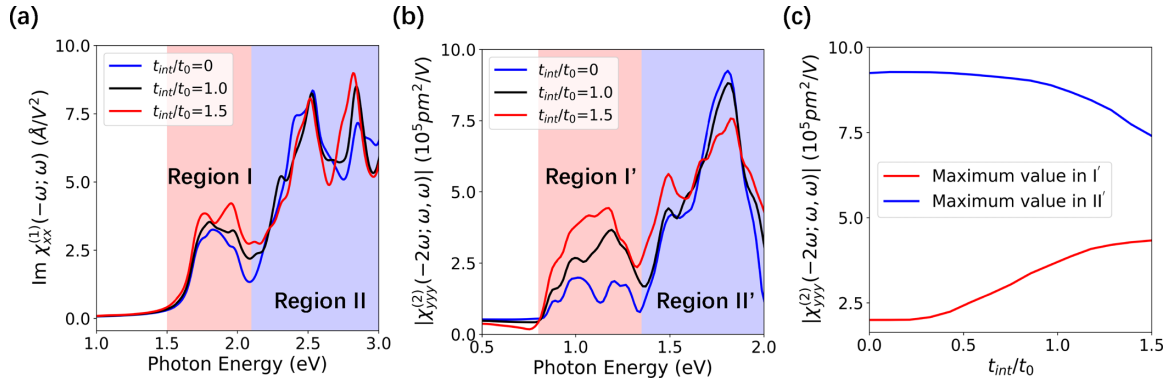


FIG. 4. (a) Linear $\text{Im}\chi^{(1)}(-\omega; \omega)$ (imaginary part of dielectric function) and (b) frequency-dependent SHG susceptibility $|\chi_{yyy}^{(2)}(-2\omega; \omega, \omega)|$ of the heterobilayer $\text{MoS}_2/\text{MoSe}_2$ with different interlayer hopping strength t_{int} . (c) Maximum values of the $|\chi_{yyy}^{(2)}(-2\omega; \omega, \omega)|$ spectra in region I' and region II' [marked in (b)] as a function of t_{int} .

valence bands and the bottom two conduction bands in the full BZ from $t_{\text{int}} = 0$ (Fig. S7(a) [42]) to $t_{\text{int}} = t_0$ (Fig. S7(b) [42]). As shown in Fig. 3(e), we can observe that the optical transitions are largely increased around the Γ point in the BZ.

Due to the C_{3v} point-group symmetry, besides of the dominated SHG susceptibility element $\chi_{yyy}^{(2)} = -\chi_{yxx}^{(2)} = -\chi_{xyx}^{(2)} = -\chi_{xyy}^{(2)}$, more nonzero SHG elements, i.e., $\chi_{zzz}^{(2)}$, $\chi_{zyy}^{(2)} = \chi_{zxx}^{(2)}$, $\chi_{xzz}^{(2)} = \chi_{yyz}^{(2)}$, appear in the $\text{MoS}_2/\text{MoSe}_2$. To simplify our discussion and also to compare with the case of $\text{MoS}_2/\text{MoS}_2$, we only present the $\chi_{yyy}^{(2)}$ in this study. It is found that, opposite to the increased TDMs, the calculated $\chi_{yyy}^{(2)}(0; 0, 0)$ of bilayer $\text{MoS}_2/\text{MoSe}_2$ decreases from 10.9×10^4 to 9.7×10^4 pm^2/V when t_{int} increases from 0 to t_0 . The SHG-weighted charge density [inset of Fig. 3(d)] shows that the $\chi_{yyy}^{(2)}(0; 0, 0)$ is mainly contributed by Mo $d_{x^2-y^2} + d_{xy}$, Mo d_{z^2} , and S p_z orbitals, regardless of the specific value of t_{int} .

Similar to the bilayer $\text{MoS}_2/\text{MoS}_2$, as shown in Figs. 3(b) and 3(d) (also see Figs. S7(c) and S7(d) for the SHG projection in the full BZ [42]), the positive and negative components of $\chi_{yyy}^{(2)}(0; 0, 0)$ in the $\text{MoS}_2/\text{MoSe}_2$ are mainly contributed by the electronic states around M and K points, respectively. As shown Fig. 3(f), when the t_{int} increases, the interlayer orbital coupling can significantly increase the negative component of $\chi_{yyy}^{(2)}(0; 0, 0)$, reducing the $\chi_{yyy}^{(2)}(0; 0, 0)$ value. As shown in Fig. 3(g), the calculated $\chi_{yyy}^{(2)}(0; 0, 0)$ value gradually decreases from 5.2×10^4 pm^2/V ($t_{\text{int}} = 0$) to 3.6×10^4 pm^2/V ($t_{\text{int}} = 1.5t_0$), a large reduction of $\sim 31\%$. Three d_{int} values corresponding to the different t_{int} are also calculated and marked in Fig. 3(g). With the t_{int} increases from $0.35t_0$ to $1.0t_0$ to $1.35t_0$, the d_{int} decreases from 4.4 to 3.2 to 2.9 \AA . Therefore, similar to the homobilayer $\text{MoS}_2/\text{MoS}_2$, we can conclude that although the increase of t_{int} can increase the TDMs, the increased band repulsion around the Γ point in the heterobilayer $\text{MoS}_2/\text{MoSe}_2$ can still decrease $\chi_{yyy}^{(2)}(0; 0, 0)$; the larger the t_{int} , the stronger band repulsion around the Γ point and consequently the smaller the $\chi_{yyy}^{(2)}(0; 0, 0)$.

D. $|\chi_{yyy}^{(2)}(-2\omega; \omega, \omega)|$ spectra of the heterobilayer $\text{MoS}_2/\text{MoSe}_2$ as a function of t_{int}

Figure 4(a) shows the calculated linear $\text{Im}\chi^{(1)}(-\omega; \omega)$ spectra for the $\text{MoS}_2/\text{MoSe}_2$. Generally, there are multiple

peaks in the low photon-energy region I ($1.5 \sim 2.1$ eV) and the high photon-energy region II ($2.1 \sim 3.0$ eV). When $t_{\text{int}} = 0$, without the interlayer interactions, the peaks in region I are mostly contributed by the band-edge optical transitions around the K point in each individual intralayer, while the interlayer optical transitions are completely forbidden (see Fig. S8(a) [42]). When $t_{\text{int}} \neq 0$, the interlayer optical transitions around the band edge appear and increase as the t_{int} increases (see Fig. S8(b) [42]), giving rise to the enhanced optical transitions in region I of $\text{Im}\chi^{(1)}(-\omega; \omega)$. On the other hand, when $t_{\text{int}} = 0$, the multiple peaks with strong intensities in region II are mostly contributed by the optical transitions around the Γ point and the band-nesting effect along part of the Γ - K line in each individual intralayer. When $t_{\text{int}} \neq 0$, the interlayer optical transitions appear in region II and increase as the t_{int} increases; meanwhile, the band-nesting effect is reduced due to the increased interlayer orbital coupling. Therefore, the coexistence of these two completing effects gives rise to a complicated evolution of these peaks in region II as a function of t_{int} .

We have further calculated the $|\chi_{yyy}^{(2)}(-2\omega; \omega, \omega)|$ spectra for three different t_{int} values, as shown in Fig. 4(b). Differing from the case of homobilayer $\text{MoS}_2/\text{MoS}_2$ [Fig. 2(b)], it is difficult to distinguish the contributions from single-photon and double-photon resonances in these spectra. Interestingly, the multiple peaks in $|\chi_{yyy}^{(2)}(-2\omega; \omega, \omega)|$ spectra can also be divided into the two regions, i.e., low phonon-energy region I' ($0.8 \sim 1.3$ eV) and high phonon-energy region II' ($1.3 \sim 2.0$ eV). When t_{int} increases, the interlayer optical transitions can significantly increase the intensities of peaks in region I'. As shown in Fig. 4(c), the maximum $|\chi_{yyy}^{(2)}(-2\omega; \omega, \omega)|$ in region I' gradually increases from 2.0×10^5 to 4.2×10^5 pm^2/V , a huge increase of $\sim 110\%$. Differing from region I', the changes of $|\chi_{yyy}^{(2)}(-2\omega; \omega, \omega)|$ in the high photon-energy region II' could be mainly contributed by the intralayer optical transitions. Especially, the SHG peak at ~ 1.8 eV is caused by the band-nesting effect along part of the K - Γ line (Fig. S5(b) [42]). The larger the t_{int} , the weaker the band-nesting effect, and consequently the weaker the $|\chi_{yyy}^{(2)}(-2\omega; \omega, \omega)|$ value at ~ 1.8 eV. As shown in Fig. 4(c), in contrast to region I, the maximum $|\chi_{yyy}^{(2)}(-2\omega; \omega, \omega)|$ value in region II' (i.e., peak value at ~ 1.8 eV) will gradually decrease from

9.2×10^5 to 7.4×10^5 , a small reduction of $\sim 20\%$. Interestingly, we emphasize that since the band-nesting effect in the heterobilayer $\text{MoS}_2/\text{MoSe}_2$ (Fig. S5(b) [42]) is weaker than that in the homobilayer $\text{MoS}_2/\text{MoS}_2$ (Fig. S5(a) [42]), the change of SHG peak intensity is also less noticeable in $\text{MoS}_2/\text{MoSe}_2$ ($\sim 20\%$) than in $\text{MoS}_2/\text{MoS}_2$ ($\sim 35\%$).

Recently, there are experimental studies on the effects of interlayer coupling on the SHG intensity in 3R-type heterobilayer $\text{MoS}_2/\text{MoSe}_{2(1-x)}\text{Se}_{2x}$ samples [26]. Interestingly, it is found that there is a strong enhancement of SHG intensity at the low photon-energy range (~ 1.0 eV) from the decoupled sample ($t_{\text{int}} \sim 0$) to the coupled one ($t_{\text{int}} = t_0$), which is very different from the observations in the homobilayer $\text{MoS}_2/\text{MoS}_2$ samples. The physical origin behind these puzzling experimental observations in the different TMDs under variable t_{int} can be well explained by our calculations.

IV. CONCLUSION

In summary, taking homobilayer $\text{MoS}_2/\text{MoS}_2$ and heterobilayer $\text{MoS}_2/\text{MoSe}_2$ as typical examples, we have systemically investigated their SHG susceptibilities $\chi^{(2)}$ as a

function of t_{int} using first-principles Wannier function calculations. For the $\chi_{yyy}^{(2)}(0; 0, 0)$ of $\text{MoS}_2/\text{MoS}_2$ and $\text{MoS}_2/\text{MoSe}_2$, it is found that the larger the t_{int} , the smaller the $\chi_{yyy}^{(2)}(0; 0, 0)$. For $|\chi_{yyy}^{(2)}(-2\omega; \omega, \omega)|$ of $\text{MoS}_2/\text{MoSe}_2$ in the low photon-energy region, differing from the $\text{MoS}_2/\text{MoS}_2$, their peak values are very sensitive to the t_{int} ; the larger the t_{int} , the larger the $|\chi_{yyy}^{(2)}(-2\omega; \omega, \omega)|$. For dynamical $|\chi_{yyy}^{(2)}(-2\omega; \omega, \omega)|$ of $\text{MoS}_2/\text{MoS}_2$ in the high photon-energy region, comparing to the $\text{MoS}_2/\text{MoSe}_2$, their peak values will gradually decrease in a much more noticeable way as the t_{int} increases. Our study not only can successfully explain the recent experimental observations on the dramatically different SHG responses in different bilayer TMDs as a function of interlayer coupling strengths, but also may provide a general approach to tune the SHG effects in the vdW bilayer systems.

ACKNOWLEDGMENTS

The authors thank J. F. Wang, Y. Li, and B. Shao for helpful discussions. This work is supported by the NSFC (Grants No. 12088101 and No. 11634003) and NSAF Grant No. U1930402. Part of the calculations were done in Tianhe-JK cluster at CSRC.

-
- [1] K. S. Novoselov, A. Mishchenko, A. Carvalho, and A. H. Castro Neto, *Science* **353**, aac9439 (2016).
- [2] J. R. Schaibley, H. Yu, G. Clark, P. Rivera, J. S. Ross, K. L. Seyler, W. Yao, and X. Xu, *Nat. Rev. Mater.* **1**, 16055 (2016).
- [3] A. Carvalho, M. Wang, X. Zhu, A. S. Rodin, H. Su, and A. H. Castro Neto, *Nat. Rev. Mater.* **1**, 16061 (2016).
- [4] P. A. Franken, A. E. Hill, C. W. Peters, and G. Weinreich, *Phys. Rev. Lett.* **7**, 118 (1961).
- [5] H. Wang and X. Qian, *Nano Lett.* **17**, 5027 (2017).
- [6] K. Yao, N. R. Finney, J. Zhang, S. L. Moore, L. Xian, N. Tancogne-Dejean, F. Liu, J. Ardelean, X. Xu, D. Halbertal, K. Watanabe, T. Taniguchi, H. Ochoa, A. Asenjo-Garcia, X. Zhu, D. N. Basov, A. Rubio, C. R. Dean, J. Hone, and P. J. Schuck, *Sci. Adv.* **7**, eabe8691 (2021).
- [7] L. Zhou, H. Fu, T. Lv, C. Wang, H. Gao, D. Li, L. Deng, and W. Xiong, *Nanomaterials (Basel)* **10**, 2263 (2020).
- [8] A. Autere, H. Jussila, Y. Dai, Y. Wang, H. Lipsanen, and Z. Sun, *Adv. Mater.* **30**, e1705963 (2018).
- [9] L. Zhao, D. H. Torchinsky, H. Chu, V. Ivanov, R. Lifshitz, R. Flint, T. Qi, G. Cao, and D. Hsieh, *Nat. Phys.* **12**, 32 (2015).
- [10] Z. Sun, Y. Yi, T. Song, G. Clark, B. Huang, Y. Shan, S. Wu, D. Huang, C. Gao, Z. Chen, M. McGuire, T. Cao, D. Xiao, W.-T. Liu, W. Yao, X. Xu, and S. Wu, *Nature (London)* **572**, 497 (2019).
- [11] R. Wang, H.-C. Chien, J. Kumar, N. Kumar, H.-Y. Chiu, and H. Zhao, *ACS Appl. Mater. Interfaces* **6**, 314 (2014).
- [12] L. M. Malard, T. V. Alencar, A. P. M. Barboza, K. F. Mak, and A. M. de Paula, *Phys. Rev. B* **87**, 201401(R) (2013).
- [13] Y. Li, Y. Rao, K. F. Mak, Y. You, S. Wang, C. R. Dean, and T. F. Heinz, *Nano Lett.* **13**, 3329 (2013).
- [14] X. Hong, J. Kim, S.-F. Shi, Y. Zhang, C. Jin, Y. Sun, S. Tongay, J. Wu, Y. Zhang, and F. Wang, *Nat. Nanotechnol.* **9**, 682 (2014).
- [15] T. Cheiwchanhangij and W. R. L. Lambrecht, *Phys. Rev. B* **85**, 205302 (2012).
- [16] D. H. Kim and D. Lim, *J. Korean Phys. Soc.* **66**, 816 (2015).
- [17] Z. Gong, G. B. Liu, H. Yu, D. Xiao, X. Cui, X. Xu, and W. Yao, *Nat. Commun.* **4**, 2053 (2013).
- [18] G. Wang, I. C. Gerber, L. Bouet, D. Lagarde, A. Balocchi, M. Vidal, T. Amand, X. Marie, and B. Urbaszek, *2D Mater.* **2**, 045005 (2015).
- [19] Z. Ye, T. Cao, K. O'Brien, H. Zhu, X. Yin, Y. Wang, S. G. Louie, and X. Zhang, *Nature (London)* **513**, 214 (2014).
- [20] H. Zeng, G.-B. Liu, J. Dai, Y. Yan, B. Zhu, R. He, L. Xie, S. Xu, X. Chen, W. Yao, and X. Cui, *Sci. Rep.* **3**, 1608 (2013).
- [21] J. Ribeiro-Soares, C. Janisch, Z. Liu, A. L. Elías, M. S. Dresselhaus, M. Terrones, L. G. Cançado, and A. Jorio, *2D Mater.* **2**, 045015 (2015).
- [22] K. Ba, W. Jiang, J. Cheng, J. Bao, N. Xuan, Y. Sun, B. Liu, A. Xie, S. Wu, and Z. Sun, *Sci. Rep.* **7**, 45584 (2017).
- [23] S. Deckoff-Jones, J. Zhang, C. E. Petoukhoff, M. K. L. Man, S. Lei, R. Vajtai, P. M. Ajayan, D. Talbayev, J. Madéo, and K. M. Dani, *Sci. Rep.* **6**, 22620 (2016).
- [24] L. Karvonen, A. Säynätjoki, S. Mehravar, R. D. Rodriguez, S. Hartmann, D. R. T. Zahn, S. Honkanen, R. A. Norwood, N. Peyghambarian, K. Kieu, H. Lipsanen, and J. Riihonen, *Sci. Rep.* **5**, 10334 (2015).
- [25] K. L. Seyler, J. R. Schaibley, P. Gong, P. Rivera, A. M. Jones, S. Wu, J. Yan, D. G. Mandrus, W. Yao, and X. Xu, *Nat. Nanotechnol.* **10**, 407 (2015).
- [26] C. T. Le, J. Kim, F. Ullah, A. D. Nguyen, T. N. N. Tran, T.-E. Le, K.-H. Chung, H. Cheong, J. I. Jang, and Y. S. Kim, *ACS Nano* **14**, 4366 (2020).
- [27] K. F. Mak, C. Lee, J. Hone, J. Shan, and T. F. Heinz, *Phys. Rev. Lett.* **105**, 136805 (2010).
- [28] Y. Zhang, T. T. Tang, C. Girit, Z. Hao, M. C. Martin, A. Zettl, M. F. Crommie, Y. R. Shen, and F. Wang, *Nature (London)* **459**, 820 (2009).

- [29] T. T. Tang, Y. Zhang, C.-H. Park, B. Geng, C. Girit, Z. Hao, M. C. Martin, A. Zettl, M. F. Crommie, S. G. Louie, Y. R. Shen, and F. Wang, *Nat. Nanotechnol.* **5**, 32 (2010).
- [30] Y. Cao, V. Fatemi, S. Fang, K. Watanabe, T. Taniguchi, E. Kaxiras, and P. Jarillo-Herrero, *Nature (London)* **556**, 43 (2018).
- [31] A. Surrente, D. Dumcenco, Z. Yang, A. Kuc, Y. Jing, T. Heine, Y.-C. Kung, D. K. Maude, A. Kis, and P. Plochocka, *Nano Lett.* **17**, 4130 (2017).
- [32] F. Ceballos, M. Z. Bellus, H.-Y. Chiu, and H. Zhao, *ACS Nano* **8**, 12717 (2014).
- [33] M. S. Kim, C. Seo, H. Kim, J. Lee, D. H. Luong, J. H. Park, G. H. Han, and J. Kim, *ACS Nano* **10**, 6211 (2016).
- [34] X. Song, J. Sun, Y. Qi, T. Gao, Y. Zhang, and Z. Liu, *Adv. Energy Mater.* **6**, 1600541 (2016).
- [35] P. Koskinen, I. Fampiou, and A. Ramasubramaniam, *Phys. Rev. Lett.* **112**, 186802 (2014).
- [36] S. Huang, G. Zhang, F. Fan, C. Song, F. Wang, Q. Xing, C. Wang, H. Wu, and H. Yan, *Nat. Commun.* **10**, 2447 (2019).
- [37] J. Xia, J. Yan, Z. Wang, Y. He, Y. Gong, W. Chen, T. C. Sum, Z. Liu, P. M. Ajayan, and Z. Shen, *Nat. Phys.* **17**, 92 (2020).
- [38] J. E. Sipe and A. I. Shkrebtii, *Phys. Rev. B* **61**, 5337 (2000).
- [39] S. N. Rashkeev, W. R. L. Lambrecht, and B. Segall, *Phys. Rev. B* **57**, 3905 (1998).
- [40] B. M. Fregoso, T. Morimoto, and J. E. Moore, *Phys. Rev. B* **96**, 075421 (2017).
- [41] C. Wang, X. Liu, L. Kang, B.-L. Gu, Y. Xu, and W. Duan, *Phys. Rev. B* **96**, 115147 (2017).
- [42] See Supplemental Material at <http://link.aps.org/supplemental/10.1103/PhysRevB.105.045415> for the SHG calculation convergence test of the smearing factor δ and number of bands; atom structures and SHG-weighted charge density of the homobilayer MoS₂/MoS₂ and the heterobilayer MoS₂/MoSe₂ in 3R phase; comparison of band structures obtained by DFT calculations and obtained by DFT+Wannier interpolation; SHG and TDMs projections for the homobilayer MoS₂/MoS₂ and the heterobilayer MoS₂/MoSe₂ under $t_{\text{int}} = 0$ and $t_{\text{int}} = t_0$ in the full BZ; JDOS under different interlayer hopping strength t_{int} in the homobilayer MoS₂/MoS₂ and the heterobilayer MoS₂/MoSe₂; comparison of experimentally measured and calculated A/2 and B/2 peaks of the decoupled homobilayer MoS₂/MoS₂; optical transition projected band structure of decoupled ($t_{\text{int}} = 0$) and coupled ($t_{\text{int}} = t_0$) bilayer MoS₂/MoSe₂ system.
- [43] M.-H. Lee, C.-H. Yang, and J.-H. Jan, *Phys. Rev. B* **70**, 235110 (2004).
- [44] R. He, Z. S. Lin, M. H. Lee, and C. T. Chen, *J. Appl. Phys.* **109**, 103510 (2011).
- [45] J. Wang, X. Sui, S. Gao, W. Duan, F. Liu, and B. Huang, *Phys. Rev. Lett.* **123**, 206402 (2019).
- [46] J. Wang, X. Sui, W. Duan, F. Liu, and B. Huang, *Proc. Natl. Acad. Sci. USA* **118**, e2023029118 (2021).
- [47] G. Kresse and J. Furthmüller, *Phys. Rev. B* **54**, 11169 (1996).
- [48] P. E. Blöchl, *Phys. Rev. B* **50**, 17953 (1994).
- [49] J. P. Perdew, K. Burke, and M. Ernzerhof, *Phys. Rev. Lett.* **77**, 3865 (1996).
- [50] S. Grimme, J. Antony, S. Ehrlich, and H. Krieg, *J. Chem. Phys.* **132**, 154104 (2010).
- [51] L. Kang, X. Liu, Z. Lin, and B. Huang, *Phys. Rev. B* **102**, 205424 (2020).
- [52] Y. Guo, H. Zhu, and Q. Wang, *J. Phys. Chem. C* **124**, 5506 (2020).
- [53] N. Marzari, A. A. Mostofi, J. R. Yates, I. Souza, and D. Vanderbilt, *Rev. Mod. Phys.* **84**, 1419 (2012).
- [54] G.-B. Liu, W.-Y. Shan, Y. Yao, W. Yao, and D. Xiao, *Phys. Rev. B* **88**, 085433 (2013).
- [55] S. Fang, R. Kuate Defo, S. N. Shirodkar, S. Lieu, G. A. Tritsarlis, and E. Kaxiras, *Phys. Rev. B* **92**, 205108 (2015).
- [56] D. Kozawa, R. Kumar, A. Carvalho, K. K. Amara, W. Zhao, S. Wang, M. Toh, R. M. Ribeiro, A. H. C. Neto, K. Matsuda, and Goki Eda, *Nat. Commun.* **5**, 4543 (2014).
- [57] M. L. Trolle, G. Seifert, and T. G. Pedersen, *Phys. Rev. B* **89**, 235410 (2014).
- [58] R. C. Miller, *Appl. Phys. Lett.* **5**, 17 (1964).